Finite element analysis of radial cooled rotating electrical machines

M.S. Rajagopal
R&D, Kirloskar Electric Co. Ltd, Bangalore, India
K.N. Seetharamu
Mechanical Engineering Department, IIT, Madras, India, and
P.A. Aswatha Narayana
Applied Mechanics Department, IIT, Madras, India

Keywords *Electrical machines, Finite element method, Thermal analysis*

Abstract *Accurate prediction of temperature distribution in an electrical machine at the design stage is becoming increasingly important. It is essential to know the locations and magnitudes of hot spot temperatures for optimum design of electrical machines. A methodology based on axi-symmetric finite element formulation has been developed to solve the conduction-convection problem in radial cooled machines using a new eight noded solid-fluid coupled element. The axi-symmetric model adopted is formulated purely from dimensional data, property data and published convective correlations. Steady state temperatures have been determined for 102kW radial cooled motor at 100 and 75 percent loads and are validated with experimental results obtained from heat run tests. Parametric studies have been carried out to study the effect of critical parameters on temperature distribution and for optimising the design.*

Nomenclature

a,b = length (m)
c = specific heat (W/kg K)
f = load matrix
G = heat generation (W)
h = heat transfer co-efficient (W/m^2 K)
k = thermal conductivity (W/m K)
K = thermal conductivity (W/m K); matrix
l_r, l_z = direction cosines
L = length (m)
m = mass (kg)
N = shape function; speed (rpm)
Pr = Prandtl number
Q = load matrix co-efficients
Q_g = heat generation per unit volume (W/m^3)
r, z = spatial cylindrical co-ordinates (m)
Re = Reynolds number
S = surface
s,t = local co-ordinate system in r and z directions
T = temperature (K)
V = volume

Subscripts
a = ambient; average
cl = convection from left wall
cond = conduction
conv = convection
cr = convection from right wall
f = fluid
fl = fluid left
fr = fluid right
h = hot
i = inner
i,j,k,m = solid nodes
l = left
n,o,p,q = fluid nodes
o = outer
r = right
r, z = cylindrical co-ordinate directions
w = wall
wl = wall left
wr = wall right

International Journal of Numerical Methods for Heat & Fluid Flow, Vol. 9 No. 1, 1999, pp. 18-38,
© MCB University Press, 0961-5539

The authors would like to express their sincere thanks to the management of Kirloskar Electric Co. Ltd, Bangalore for giving permission to publish this work.

1. Introduction

With increasing material costs there has been a tendency to reduce the frame size of the machines for a given output or to enhance the ratings for a given frame size. The margin of error in thermal design of electrical machines is often small and hence there is an increased need for accurate analysis of thermal problems. Prediction of temperature distribution enables a designer to optimise the design and hence effect cost savings. This will also reduce prototype testing of a series of machines in addition to reducing lead time for development of new machines. Steady state temperature rise is important to determine the continuous rating of the machine. To ensure satisfactory working, stator winding temperatures must be below the designed insulation class limit and rotor temperatures must be limited to prevent fatigue and mechanical distortion.

Most of the earlier researchers and designers have traditionally adopted either the thermal resistance network method or the finite difference method for prediction of temperatures. The resistance method predicts the average temperatures quite accurately but fails in predicting the hot spot temperatures. The finite difference method, unlike the resistance method, is capable of predicting the hot spots, but cannot handle complex geometries.

Use of the finite element method for the solution of heat flow has had wide acceptance among researchers in recent years. Armor and Chari (1976) have used the finite element method to analyse stator core heating of a large turbine generator and the results are compared with resistance analog methods and test results. They have ignored the heating effect of stator coils and used temperature boundary conditions instead of convective boundary conditions.

Chari and Armor (1977) have used hybrid finite element analysis for solving the combined magnetic field and temperature distribution problems. A 2-D non-linear finite element magnetic field model is used to obtain core losses. The thermal part is similar to their earlier work (Armor and Chari, 1976). For analysing the magnetic field problem, they have assumed the magnetic vector potential to be invariant in the axial direction. They have considered only a slice of the stator core and assumed that the core is unaffected by the end effects. They have used first order triangular finite elements for the magnetic field problem.

Nonaka *et al.* (1981) have provided an analytical method for determining the ventilation and cooling in radial cooled induction motors. They have solved the cooling problem using a quasi three-dimensional steady state thermal analysis with the help of the finite element method and validated their theoretical results with experiments conducted on a four pole 600kW motor. Parametric studies on the stator design have also been carried out. However, they have neglected rotor and stator heat interaction.

Ohishi *et al.* (1987) have analysed the effects of severe unbalanced current distribution in the stator coils of electrical machines. They have calculated the losses in a single coil and used a network model to determine the temperature

distribution in the coils. They have modelled half a slot and half a tooth with fluid nodes. The predicted results have been compared with experimental results. This work does not consider rotor heat interaction.

Witczak (1986) has predicted the transient temperature distribution in the stator windings and core of the stator during starting conditions using a quasi-analytical method of calculation. The analysis is carried out in a two-dimensional model containing only one slot pitch of the stator with many assumptions. It is assumed that the whole stator coil and stator core surface are at the same temperature. Further, the heat interaction between rotor and stator is neglected.

Stephenson (1989) in his work has determined the temperature rise of rotor windings of large radial cooled generators. The effect of asymmetric temperature distribution with the consequent thermal stresses and deformation of the rotor results in rotor vibration. This work makes use of a three-dimensional lumped scheme to model the rotor. The heat interaction of stator and rotor has not been considered.

Williamson and Walker (1991) have used 2-D time stepping finite difference scheme to solve the thermal transient problem. A 2-D thermal network model of a rotor bar and its surrounding core is considered to predict rotor bar temperatures. In this work, the interaction between the rotor bars and core has been considered, but the rotor-stator interaction has been neglected.

Rajagopal *et al.* (1998) have carried out transient thermal analysis of totally enclosed fan ventilated (TEFV) induction motors using the finite element method and validated the predictions by experiments. The formulation of TEFV machines involves conduction phenomenon only whereas the radial cooled machines (RCM) involves both conduction and convection.

Most of the heat transfer studies have been restricted to steady state and transient analysis of either single stator or single rotor slot pitch. It has been observed that the rotor-stator heat interaction has not been considered in the literature. The present work analyses the radial cooled machine as a system with heat generation in both rotor and stator.

2. Thermal modelling

The models adopted by earlier researchers varied from very simple lumped parameter method to very detailed finite element studies, but with some loss of essential physical details. The proposed axi-symmetric thermal model can easily accommodate all the main heat transfer processes without simplifying the necessary geometric details. In this approach, the main assumptions are that the isotherms are essentially circular and centred on the rotor axis.

The schematic of the axi-symmetric model of a radial cooled motor along with the flow paths is shown in Figure 1. The heat transfer phenomenon in a radial cooled machine is predominantly by forced convection. The internal fans force the air into the rotor and stator and directly cool them. The cooling medium after taking away the heat from rotor-stator system is cooled in the

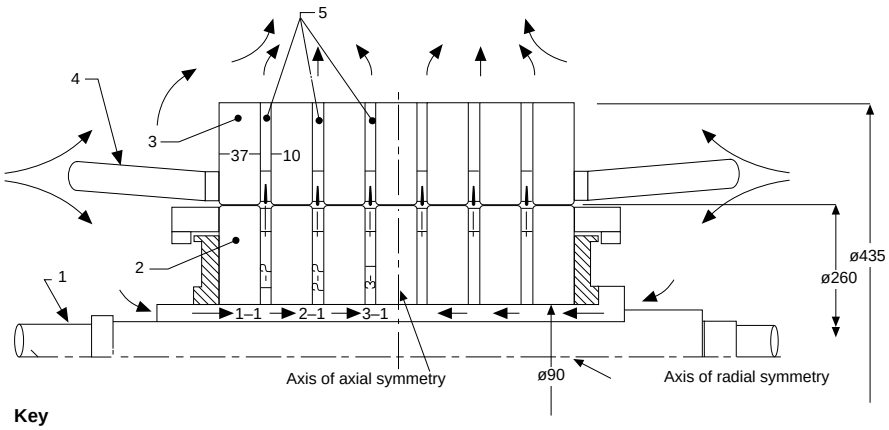

Key

1. Shaft
2. Rotor core pack
3. Stator core pack
4. Stator winding overhang
5. Radial ducts

Figure 1.
Thermal model of radial cooled motor

heat exchanger and recirculated. To analyse such a system, one should know the flow rates inside the various sections of the machine from which the convective heat transfer co-efficients can be determined. It is also necessary to know the extent of cooling in the heat exchanger. These two form the boundary conditions for the solid and fluid respectively in the thermal problem. For discretisation, it is necessary to consider both the solid and fluid regions together. This concept has been instrumental in proposing an eight noded coupled solid-fluid element which can be used to discretise the domain.

The model basically consists of annular regions comprising shaft, rotor core, rotor winding, air gap, stator winding and stator core. Only temperature distribution in the r-z plane is evaluated due to rotational symmetry. The non-homogeneous laminated nature of the rotor and stator iron is represented by using different values of thermal conductivities in radial and axial directions. The temperature field is assumed continuous (i.e. no contact resistance) and the heat sources are defined for rotor winding, stator winding and stator core regions. Insulated boundary conditions are assumed at the inner and outer cylindrical surfaces.

2.1 Convective heat transfer coefficients in radial ducts

The effect of rotation of the rotor on the duct heat transfer co-efficients has been studied by many researchers. However, most of the experimental works have been restricted to low speeds which are applicable to only large turbo-generators. Earlier designers had neglected the effect of rotor rotation on radial ducts, which resulted in pessimistic designs. Nonaka *et al.* (1981) have taken velocity ratios between two to three due to rotor rotation for determination of heat transfer co-efficients. The co-efficients of heat transfer in the ducts of radial cooled machines can be obtained from Colburn's equation,

$$h = 0.023\, Re^{0.8}\, Pr^{1/3}\, \frac{k}{d} \quad (1)$$

where, h = heat transfer coefficient, Pr = Prandtl number and k = thermal conductivity of air

$$Re = \frac{ud}{\nu} \quad (2)$$

where u = flow velocity in the duct, ν = kinematic viscosity of air and the equivalent diameter (d) is given by, $d = \frac{4 \times (\text{cross} - \text{sectional area of duct})}{\text{wetted perimeter}}$

In the present work, the rotor rotation on the duct heat transfer co-efficients has been effected by multiplying the rotor and stator duct heat transfer co-efficients obtained from equation (1) by the factors KROT and KSTAT respectively. These factors have been determined by matching the numerical results with experimental values. The factors KROT and KSTAT at 3,000 rpm used in the present analysis are 2.4 and 1.9 respectively. The heat transfer co-efficients in the radial ducts vary along the radial duct as the radius changes. The heat transfer co-efficients at each nodal location in the duct at 3,000 rpm in the radial cooled motor are given in Table I. The heat transfer co-efficients listed are the enhanced values considering the effect of rotation.

2.2 Discretisation

Axi-symmetry is used to discretise rotor-stator system. Owing to the axial symmetry, only one half of the model is considered. Discretisaton is done for both solid and fluid regions. The solid regions are discretised by using a four noded axi-symmetric quadrilateral element. The fluid flowing on either side of the solid is discretised by two noded one-dimensional linear elements. The effect of stator winding overhang has been separately considered and the losses are distributed to the corresponding nodes. The finite element mesh of radial cooled motor is shown in Figure 2.

Table I.
Duct heat transfer co-efficients in radial cooled motor

Nodal locations in FEM[a] mesh	Heat transfer co-efficient (W/m2K)
7	100.7
8	50.4
12	43.7
16	43.1
20	36.4
24	28.5

Note: [a]Figure 2 gives the nodal locations

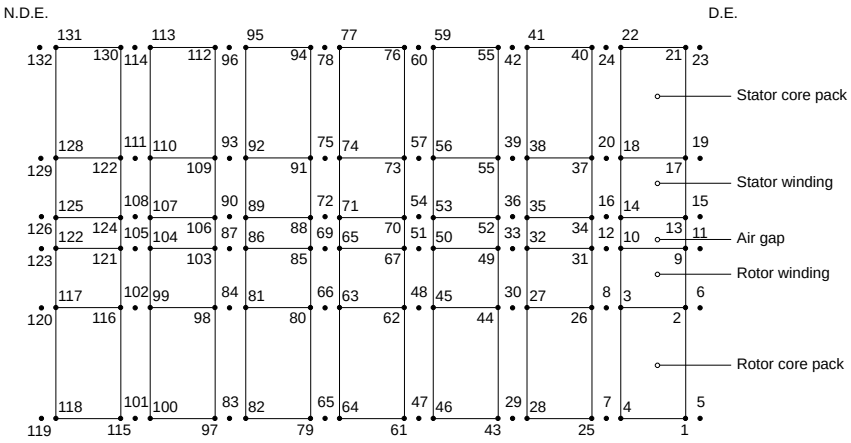

Figure 2.
Finite element mesh of radial cooled motor (with node numbers)

3. Governing equations

Figure 3 shows a typical coupled element along with the heat transfer modes from both the walls. The corresponding mapped two-dimensional domain is shown in Figure 4. The governing equations of heat transfer in a cylindrical core pack are obtained by performing an energy balance on a control volume in the solid and the fluid regions.

Under steady state conditions, considering the control volume 1234 (Figure 3),

$$Q_{cond} = -K_r(2\pi r dz)\frac{\partial T}{\partial r} - \left\{-K_r(2\pi r dz)\frac{\partial T}{\partial r} + \frac{\partial}{\partial r}\left(-K_r 2\pi r dz \frac{\partial T}{\partial r}\right)dr\right\}$$

$$-K_z(2\pi r dr)\frac{\partial T}{\partial z} - \left\{-K_z(2\pi r dr)\frac{\partial T}{\partial z} + \frac{\partial}{\partial z}\left(-K_z 2\pi r dr \frac{\partial T}{\partial z}\right)dz\right\} \quad (3)$$

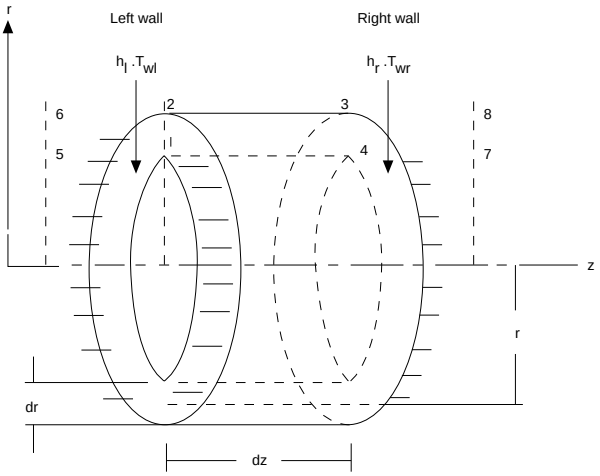

Figure 3.
3-D view of axi-symmetric coupled element; 1234 – solid control volume; 56 – fluid control volume at left; 78 – fluid control volume at right

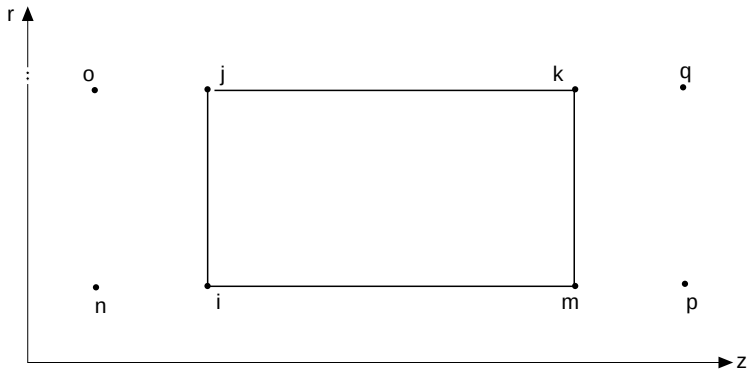

Figure 4.
Mapped 2-D domain of coupled element

$$\therefore Q_{cond} = \frac{\partial}{\partial r}\left(K_r 2\pi r dz \frac{\partial T}{\partial r}\right)dr + \frac{\partial}{\partial z}\left(K_z 2\pi r dr \frac{\partial T}{\partial z}\right)dz$$

$$\Rightarrow K_r(2\pi dr dz)\frac{\partial}{\partial r}\left(r\frac{\partial T}{\partial r}\right) + K_z 2\pi r dr dz \frac{\partial^2 T}{\partial z^2} \quad (4)$$

The heat generated from the core pack is

$$G = Q_g \cdot 2\pi r dr dz \quad (5)$$

The heat convected from left wall is

$$Q_{cl} = h_l\, 2\pi r dr (T_{wl} - T_{fl}) \quad (6)$$

The heat convected from the right wall is

$$Q_{cr} = h_r\, 2\pi r dr (T_{wr} - T_{fr}) \quad (7)$$

For steady state, sum of all thermal inputs and outputs should be equal to zero.

$$Q_{cond} + G - Q_{conv} = 0$$

$$\left(K_r 2\pi dr dz r \frac{\partial^2 T}{\partial r^2} + K_r 2\pi dr dz \frac{\partial T}{\partial r} + K_z 2\pi r dr dz \frac{\partial^2 T}{\partial z^2}\right) + Q_g 2\pi r dr dz \quad (8)$$

$$-h_l\, 2\pi r dr (T_{wl} - T_{fl}) - h_r\, 2\pi r dr (T_{wr} - T_{fr}) = 0 \quad (9)$$

Dividing throughout by $dV = 2\pi r dr dz$, we get the governing differential equation as,

$$K_r \frac{\partial^2 T}{\partial r^2} + K_r \frac{1}{r}\frac{\partial T}{\partial r} + K_z \frac{\partial^2 T}{\partial z^2} + Q_g - \frac{h_l}{L_z}(T_{wl} - T_{fl}) - \frac{h_r}{L_z}(T_{wr} - T_{fr}) = 0 \quad (10)$$

where, $L_z = dz$ is thickness in z direction.

Consider the fluid control volume (Figure 3), the governing equation for fluid at the left wall is

$$(mc)_l \frac{dT_{fl}}{dr} - h_l 2\pi r dr (T_{wl} - T_{fl}) = 0 \quad (11)$$

while the governing equation for fluid at the right wall is

$$(mc)_r \frac{dT_{fr}}{dr} - h_r 2\pi r dr (T_{wr} - T_{fr}) = 0 \quad (12)$$

4. Finite element formulation

The finite element formulation of the governing equations is carried out by Galerkin's weighted residual technique. The nodal co-ordinate details of the axi-symmetric quadrilateral element are given in Figure 5.

The solid temperature T is approximated by the interpolation function as

$$T = N_i T_i + N_j T_j + N_k T_k + N_m T_m$$

where the shape functions N_i, N_j, N_k and N_m are given by

$$N_i = \left(1 - \frac{s}{2b}\right)\left(1 - \frac{t}{2a}\right),\ N_j = \frac{s}{2b}\left(1 - \frac{t}{2a}\right)$$

$$N_k = \frac{st}{4ab} \text{ and } N_m = \frac{t}{2a}\left(1 - \frac{s}{2b}\right) \quad (13)$$

where, $s = r - r_i$ and $t = z - z_i$.

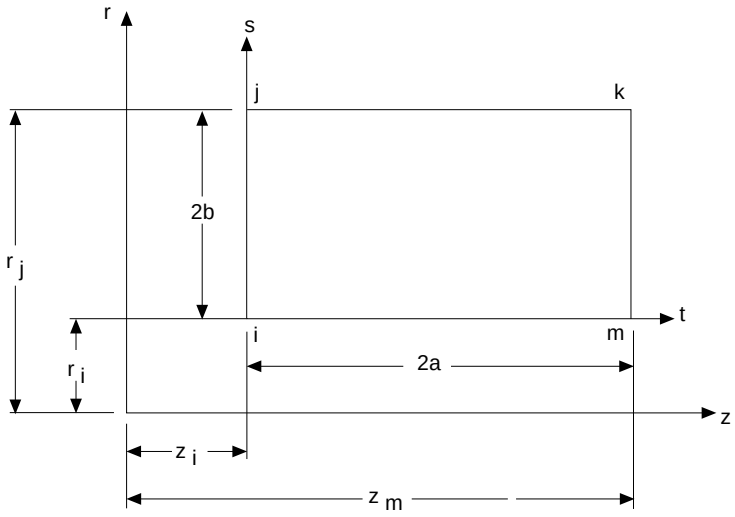

Figure 5.
Co-ordinate details of quadrilateral element of r-z plane

The nodal co-ordinate details for linear 1-D element are given in Figure 6. The shape functions for the linear 1-D element are given by

$$N_i = \left(1 - \frac{s}{L}\right) \quad \text{and} \quad N_j = \frac{s}{L} \tag{14}$$

The Galerkin's weighted residual integral for equation (10) is given by,

$$\int_V N^T \left[\frac{K_r}{r}\frac{\partial}{\partial r}\left(\frac{r\partial T}{\partial r}\right) + K_z\frac{\partial^2 T}{\partial z^2} + Q_g - \frac{h_l}{L_z}(T_{wl} - T_{fl}) - \frac{h_r}{L_z}(T_{wr} - T_{fr}) \right] dV = 0 \tag{15}$$

Since the assumed temperature profile does not have continuous first order derivatives, the second order derivatives have to be converted to first order derivatives using the product rule for differentiation and Gauss theorem. The residual integral of the first three terms of equation (15) after integration by parts is given by

$$-\int_V \left\{ \left(K_r \frac{\partial [N]^T}{\partial r}\frac{\partial T}{\partial r} + K_z \frac{\partial [N]^T}{\partial z}\frac{\partial T}{\partial z} \right) - [N]^T Q_g \right\} dV$$

$$+\int_\Gamma [N]^T \left(K_r \frac{\partial T}{\partial r} l_r + K_z \frac{\partial T}{\partial z} l_z \right) d\Gamma \tag{16}$$

Since $T^{(e)} = [N]\{T^{(e)}\}$

$$\frac{\partial T}{\partial r} = \frac{\partial [N]}{\partial r}\left\{T^{(e)}\right\}, \frac{\partial T}{\partial z} = \frac{\partial [N]}{\partial z}\left\{T^{(e)}\right\} \tag{17}$$

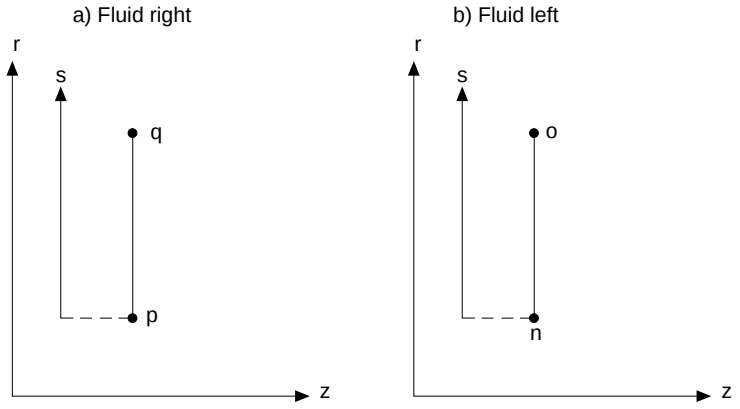

Figure 6.
Co-ordinate details of 1-D linear element

Substituting equation (17) in equation (16) gives

$$-\int_V \left\{ K_r \frac{\partial [N]^T}{\partial r}\frac{\partial [N]}{\partial r} + K_z \frac{\partial [N]^T}{\partial z}\frac{\partial [N]}{\partial z} \right\} \{T^{(e)}\} dV + \int_V Q_g [N]^T dV + \int_\Gamma [N]^T \left(K_r \frac{\partial T}{\partial r} l_r + K_z \frac{\partial T}{\partial z} l_z \right) d\Gamma \quad (18)$$

First integral multiplied by $\{T^{(e)}\}$ gives the stiffness matrix.

Substituting for the shape functions and after carrying out the integration, the stiffness matrix becomes

$$-\frac{K_r a 2\pi \bar{r}}{6b}\begin{bmatrix} 2 & -2 & -1 & 1 \\ -2 & 2 & 1 & -1 \\ -1 & 1 & 2 & -2 \\ 1 & -1 & -2 & 2 \end{bmatrix} - \frac{K_z b 2\pi \bar{r}}{6a}\begin{bmatrix} 2 & 1 & -1 & -2 \\ 1 & 2 & -2 & -1 \\ -1 & -2 & 2 & 1 \\ -2 & -1 & 1 & 2 \end{bmatrix} \quad (19)$$

where

$$\bar{r} = \frac{(r_i + r_j + r_k + r_m)}{4}$$

The integral containing Q_g is the load matrix $\{f^{(e)}\}$.

The load term after integration is

$$\frac{2\pi Q_g ab}{9}\begin{bmatrix} 4 & 2 & 1 & 2 \\ 2 & 4 & 2 & 1 \\ 1 & 2 & 4 & 2 \\ 2 & 1 & 2 & 4 \end{bmatrix}\begin{Bmatrix} r_i \\ r_j \\ r_k \\ r_m \end{Bmatrix} \quad (20)$$

The surface integral is the inter-element requirement for interior element boundaries and the derivative boundary conditions for the boundaries on Γ. The derivative boundary condition has been explicitly considered in the governing equation (10).

i.e. $$-\left[\frac{h_l}{L_z}(T_{wl} - T_f) + \frac{h_r}{L_z}(T_{wr} - T_r)\right]$$

Considering the weighted residual of the boundary condition at the left wall,

$$-\int_{\Gamma} h_l[N]^T(T_{wl} - T_{fl})d\Gamma \tag{21}$$

Since

$$T_{wl} = [N]\{T_{wl}^{(e)}\} \text{ and } T_{fl} = [N]\{T_{fl}^{(e)}\} \tag{22}$$

where

$$[N] = [N_i N_j] = \left[\left(1 - \frac{s}{L}\right) \quad \frac{s}{L}\right]$$

Considering the first term in equation (21)

$$-\int_{\Gamma} h_l[N]^T[N]\{T_{wl}^{(e)}\}d\Gamma = -\int_{\Gamma} h_l[N]^T[N]\begin{Bmatrix} T_i \\ T_j \end{Bmatrix}d\Gamma \tag{23}$$

Carrying out the integration, we get

$$-\frac{2\pi h_l L}{12}\begin{bmatrix} 3r_i + r_j & r_i + r_j \\ r_i + r_j & r_i + 3r_j \end{bmatrix}\begin{Bmatrix} T_i \\ T_j \end{Bmatrix} \tag{24}$$

Similarly, the second term in equation (21) after integration becomes

$$\frac{2\pi h_l L}{12}\begin{bmatrix} 3r_n + r_o & r_n + r_o \\ r_n + r_o & r_n + 3r_o \end{bmatrix}\begin{Bmatrix} T_n \\ T_o \end{Bmatrix} \tag{25}$$

Combining equations (24) and (25), we get

$$\frac{-2\pi h_l L}{12}\begin{bmatrix} 3r_i + r_j & r_i + r_j \\ r_i + r_j & r_i + 3r_j \end{bmatrix}\begin{Bmatrix} T_i \\ T_j \end{Bmatrix} + \frac{2\pi h_l L}{12}\begin{bmatrix} 3r_n + r_o & r_n + r_o \\ r_n + r_o & r_n + 3r_o \end{bmatrix}\begin{Bmatrix} T_n \\ T_o \end{Bmatrix} \tag{26}$$

Similarly, the weighted residual for the boundary condition at the right wall is

$$-\int_{\Gamma} h_r N^T(T_{wr} - T_{fr})d\Gamma =$$

$$-\frac{2\pi h_r L}{12}\begin{bmatrix} 3r_m + r_k & r_m + r_k \\ r_m + r_k & r_m + 3r_k \end{bmatrix}\begin{Bmatrix} T_m \\ T_k \end{Bmatrix} + \frac{2\pi h_r L}{12}\begin{bmatrix} 3r_p + r_q & r_p + r_q \\ r_p + r_q & r_p + 3r_q \end{bmatrix}\begin{Bmatrix} T_p \\ T_q \end{Bmatrix} \tag{27}$$

Galerkin's formulation of equation (11) for fluid-left is given by

$$\int [N]^T [(mc)_l \frac{dT_{fl}}{dr}] dr - \int_{\Gamma} [N]^T h_{lb}(T_{wl} - T_{fl}) d\Gamma = 0 \quad (28)$$

After integrating and simplifying, the first term in equation (28) becomes

$$\left(\frac{mc}{2}\right)_l \begin{bmatrix} -1 & 1 \\ -1 & 1 \end{bmatrix} \begin{Bmatrix} T_a \\ T_o \end{Bmatrix} \quad (29)$$

The second term in equation (28) is similar to that of equation (21) and its Galerkin's formulation, which is similar to equation (26), is

$$-E_l \begin{bmatrix} (3r_i + r_j) & (r_i + r_j) \\ (r_i + r_j) & (r_i + 3r_j) \end{bmatrix} \begin{Bmatrix} T_i \\ T_j \end{Bmatrix} + E_l \begin{bmatrix} (3r_a + r_o) & (r_a + r_o) \\ (r_a + r_o) & (r_a + 3r_o) \end{bmatrix} \begin{Bmatrix} T_a \\ T_o \end{Bmatrix} \quad (30)$$

where

$$E_l = \frac{2\pi h_{lb}}{12}$$

Combining equations (29) and (30), we get

$$\begin{bmatrix} -C_l + E_l(3r_a + r_o) & C_l + E_l(r_a + r_o) \\ -C_l + E_l(r_a + r_o) & C_l + E_l(r_a + 3r_o) \end{bmatrix} \begin{Bmatrix} T_a \\ T_o \end{Bmatrix} - E_l \begin{bmatrix} (3r_i + r_j) & (r_i + r_j) \\ (r_i + r_j) & (r_i + 3r_j) \end{bmatrix} \begin{Bmatrix} T_i \\ T_j \end{Bmatrix} \quad (31)$$

where

$$C_l = \left(\frac{mc}{2}\right)_l$$

Similarly, Galerkin's formulation for equation (12) for fluid-right results in

$$\begin{bmatrix} -C_r + E_r(3r_p + r_q) & C_r + E_r(r_p + r_q) \\ -C_r + E_r(r_p + r_q) & C_r + E_r(r_p + 3r_q) \end{bmatrix} \begin{Bmatrix} T_p \\ T_q \end{Bmatrix} - E_r \begin{bmatrix} (3r_m + r_k) & (r_m + r_k) \\ (r_m + r_k) & (r_m + 3r_k) \end{bmatrix} \begin{Bmatrix} T_m \\ T_k \end{Bmatrix} \quad (32)$$

where

$$C_r = \left(\frac{mc}{2}\right)_r \text{ and } E_r = \frac{2\pi h_{rb}}{12}$$

Combining equations (19), (20), (26), (27), (28), (31) and (32), we get the final matrix as in equation (33).

$$
\begin{bmatrix}
2(D_r + D_z) + E_i(3r_i + r_j) & -2D_r + D_z + E_i(r_i + r_j) & -(D_r + D_z) & D_r - 2D_z & -E_i(3r_a + r_o) & -E_i(r_a + r_o) & 0 & 0 \\
-2D_r + D_z + E_i(r_i + r_j) & 2(D_r + D_z) + E_i(r_i + 3r_j) & D_r - 2D_z & -(D_r + D_z) & -E_i(r_a + r_o) & -E_i(r_a + 3r_o) & 0 & 0 \\
-(D_r + D_z) & D_r - 2D_z & 2(D_r + D_z) + E_r(3r_k + r_m) & -2D_r + D_z + E_r(r_k + r_m) & 0 & 0 & -E_r(r_p + r_q) & -E_r(r_p + 3r_q) \\
D_r - 2D_z & -(D_r + D_z) & -2D_r + D_z + E_r(r_k + r_m) & 2(D_r + D_z) + E_r(3r_k + r_m) & 0 & 0 & -E_r(3r_p + r_q) & -E_r(r_p + r_q) \\
-E_i(3r_i + r_j) & -E_i(r_i + r_j) & 0 & 0 & -C_b + E_i(3r_a + r_o) & C_b + E_i(r_a + r_o) & 0 & 0 \\
-E_i(r_i + r_j) & -E_i(r_i + 3r_j) & 0 & 0 & -C_b + E_i(r_a + r_o) & C_b + E_i(r_a + 3r_o) & 0 & 0 \\
0 & 0 & -E_r(r_m + r_k) & -E_r(3r_m + r_k) & 0 & 0 & -C_t + E_r(3r_p + r_q) & C_b + E_r(r_p + r_q) \\
0 & 0 & -E_r(r_m + 3r_k) & -E_r(r_m + r_k) & 0 & 0 & -C_t + E_r(r_p + r_q) & -C_t + E_r(r_p + 3r_q)
\end{bmatrix}
\begin{Bmatrix} T_i \\ T_j \\ T_k \\ T_m \\ T_a \\ T_o \\ T_p \\ T_q \end{Bmatrix}
=
\begin{Bmatrix} Q_i \\ Q_j \\ Q_k \\ Q_m \\ 0 \\ 0 \\ 0 \\ 0 \end{Bmatrix}
\tag{33}
$$

where, $Q_i = F(4r_i + 2r_j + r_k + 2r_m)$, $Q_j = F(2r_i + 4r_j + 2r_k + r_m)$, $Q_k = F(r_i + 2r_j + 4r_k + 2r_m)$, $Q_m = F(2r_i + r_j + 2r_k + 4r_m)$ $F = \frac{2\pi Q_g ab}{9}$, $D_r = \frac{K_r a 2\pi\bar{r}}{6b}$ and $D_z = \frac{K_z b 2\pi\bar{r}}{6a}$

5. Test set up

A radial cooled induction motor has been specially designed and built to study the steady state performance. The details of the heat run tests conducted on the RCM at different loads are given below:

- 102kW (100 percent load) and 77kW (75 percent load) at 3,000 rpm.

The motor is energized and full load is applied using a DC machine. The load is regulated throughout the test to ensure constant output power. The motor is allowed to run until thermal stability is reached. The stability criterion is that the rate of change of temperature should not exceed 1.0°C/hour. The body and ambient temperatures, input power, line voltage, line current and rotor speed are recorded at 30 minute intervals during each test. A power analyser is used to measure current, voltage, power and power factor. After ensuring thermal stability, the motor is switched off and the hot stator winding resistance of all the three phases are measured. The average value of the resistance is used to calculate the stator winding temperature rise.

6. Results and discussion

The numerical results by the finite element method are validated with limited experimental data obtained from heat run tests conducted on the actual motor at 100 percent load (102kW) and 75 percent load (77kW) at the rated speed of 3,000 rpm. For prediction of temperatures, losses obtained from measurements have been used. The mesh (Figure 2) used for computation has 134 nodes and 35 elements. Grid sensitivity studies have shown that the discretisation is adequate. Parametric studies using the finite element model have also been carried out to study the effect of critical design parameters on temperature distribution.

6.1 Steady state thermal performance

The steady state thermal performance is important for determining the continuous duty rating of the machines. For a satisfactory design, the hot spots in the winding must remain below the designated insulation class limit and the rotor temperatures must be limited to prevent mechanical distortion or fatigue. The predicted results of the radial cooled motor at different loads of 100 percent and 75 percent are presented in Figures 7 and 8.

The comparison of predicted and measured temperature rise of stator winding is presented in Table II. The temperature rises of the stator winding measured by the resistance method in 100 percent and 75 percent load tests are

Test results	Predicted winding rise (°C)	Measured winding rise (°C)
100 percent load (102kW)	115.6	111.9
75 percent load (77kW)	80.6	77.7

Table II.
Comparison of predicted and measured stator winding temperature rise

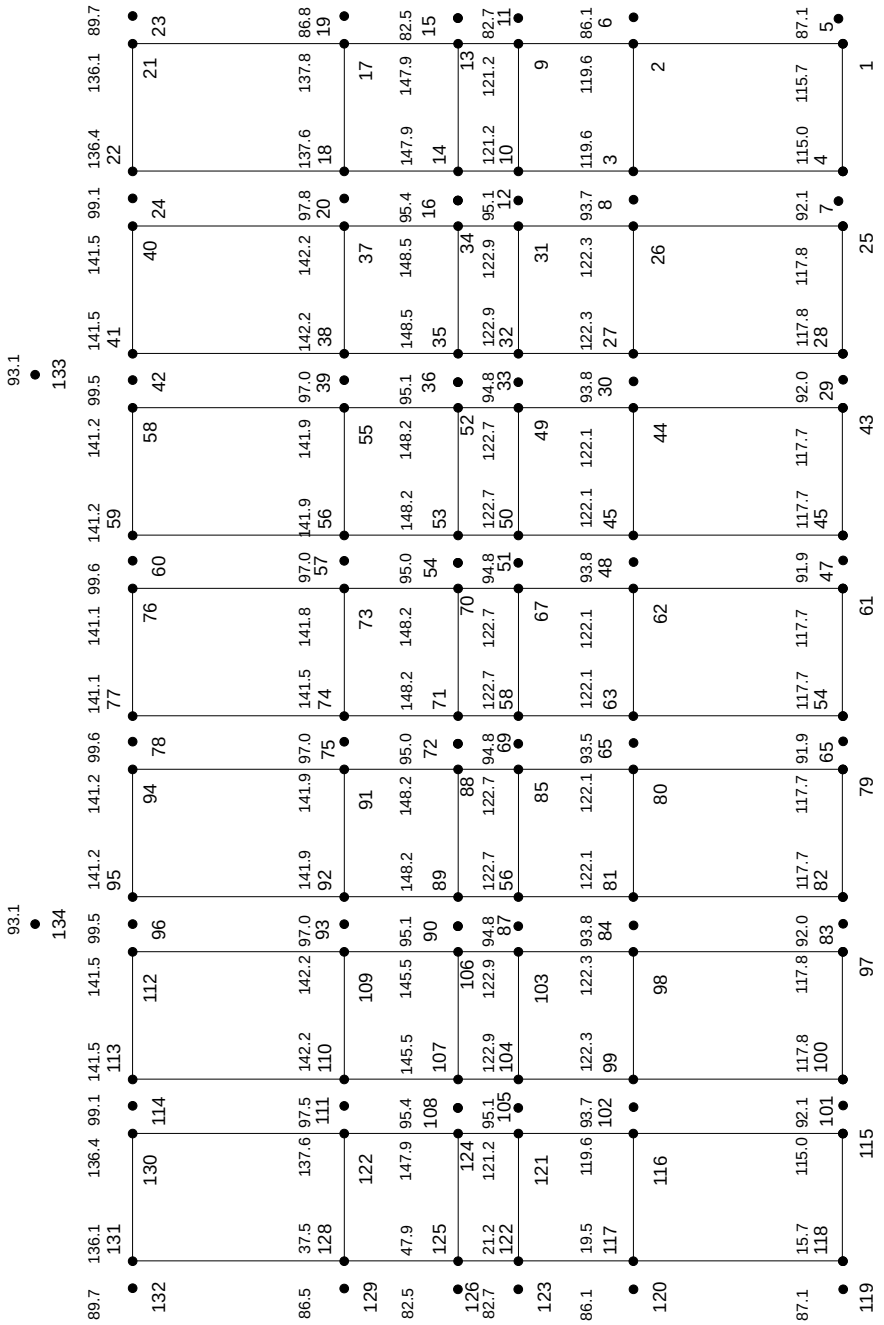

Figure 7.
Nodal temperature distribution for 100 percent load test

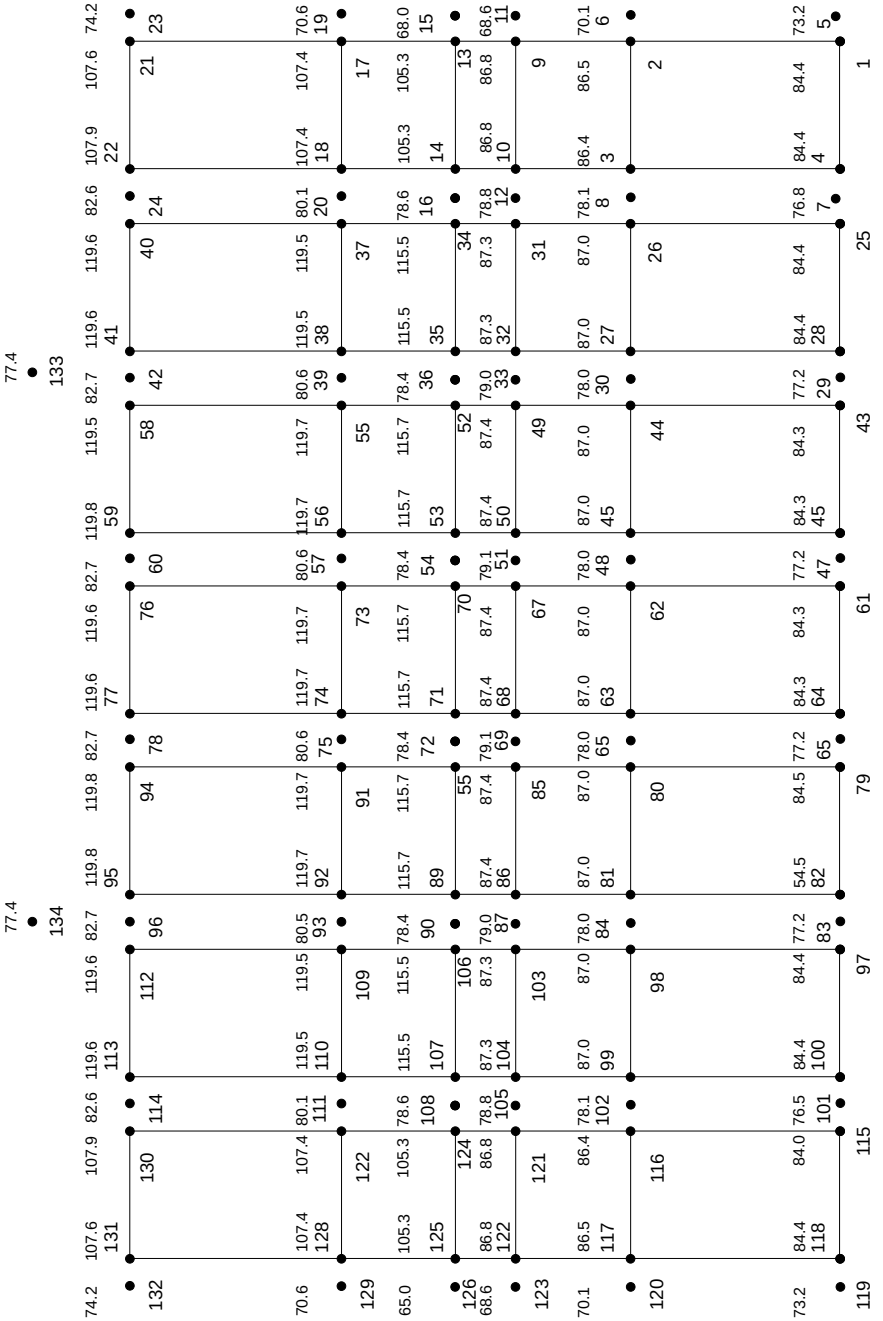

Figure 8.
Nodal temperature distribution for 75 percent load test

111.9°C and 77.7°C. This represents truly the average temperature rise of the stator winding. The corresponding predicted average temperature rises of all the nodal temperatures in the stator winding region are 115.6°C and 80.6°C for 100 percent and 75 percent load tests. It is observed that the variation between the measured winding temperature and the prediction by the finite element method (FEM) is of the order of 3 percent for both the tests.

It is observed that the predicted hot spots occur at the interior stator winding locations (nodes 34, 35, 52, 53 and 70) in 100 percent load test whereas the hot spots occur at the interior stator core region (nodes 40, 41, 58, 59 and 76) in 75 percent load test. The reasons for this behavior are that the stator iron (constant) losses remain constant for both tests whereas the stator and rotor copper losses are higher for the full load test. Hence, the heat generation in the stator core remains the same whereas it reduces in the stator and rotor windings for the 75 percent load test. The predicted results by FEM are conservative. Also, the temperatures of the interior locations of winding and core are higher than their respective locations at the ends in both the load tests. This is because the flow rates are higher at the ends and the air at entry is cooler.

6.2 Parametric studies

The effect of the critical design parameters on the thermal model of radial cooled machines is investigated. The locations of the nodes referred to in the discussions are as in Figure 2. The ranges of the parameters are also given:

- total flow rate in the internal air circuit ($0.15m^3/s$-$0.35m^3/s$)
- inlet fluid temperature (72.5°C-92.5°C)
- rotor winding loss density ($200kW/m^3$-$400kW/m^3$)
- stator duct heat transfer co-efficient ($20W/m^2K$-$60W/m^2K$).

Figure 9 shows the effect of variation of total flow rate on the temperature distribution. The designed values of total flow rate are $0.25m^3$/sec(3,000 rpm). Since total flow rate is the sum of rotor flow rate and stator flow rate, it is found that an increase in total flow rate increases both the rotor and stator flow rates. A change in total flow rate from 0.15 to 0.35 m^3/sec reduces temperatures of the interior stator winding (node 34) and interior core pack (node 40) by 27 percent and that of the rotor winding (node 31) by 22 percent respectively. The temperatures have reduced in the stator winding (node 13), core (node 21), rotor winding (node 9) and exit fluid temperature (node 133) by 8 percent, 10 percent, 14 percent and 11 percent respectively. The total flow rate affects the interior locations more than the locations at the ends. However, higher flow rate means bigger fan and poorer efficiency. This study further helps in determining the optimum flow rates for a given machine.

The effect of inlet fluid temperature on the temperature distribution is shown in Figure 10. It is observed that the temperatures at all locations vary linearly with inlet fluid temperature and the slopes of the curves are almost constant.

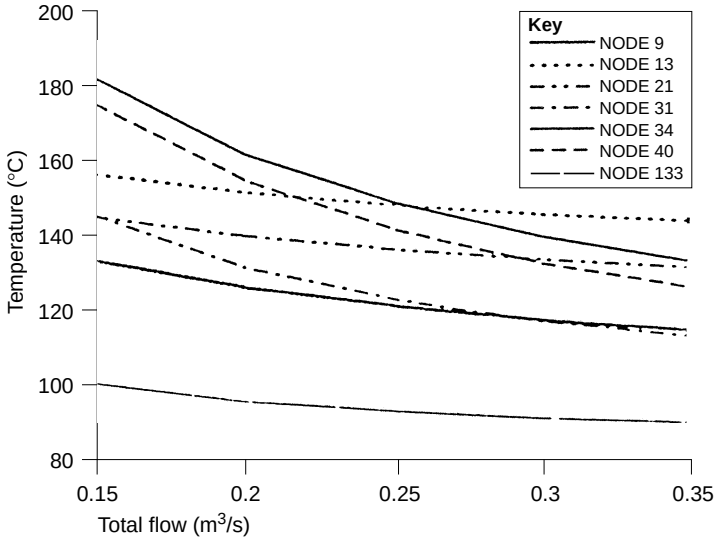

Figure 9.
Effect of total flow

An increase of 20°C in inlet fluid temperature results in a uniform increase of about 19°C in all the locations. The inlet fluid temperature forms the boundary condition for prediction of temperatures and is controlled by heat exchanger design parameters.

The effect of loss density in the rotor winding on temperature distribution is shown in Figure 11. It is seen that the rotor winding temperatures (nodes 9 and 31) increase by about 21 percent and 18 percent whereas the stator winding temperature (node 34) increases by 3.2 percent for an increase from 200kW/m^3

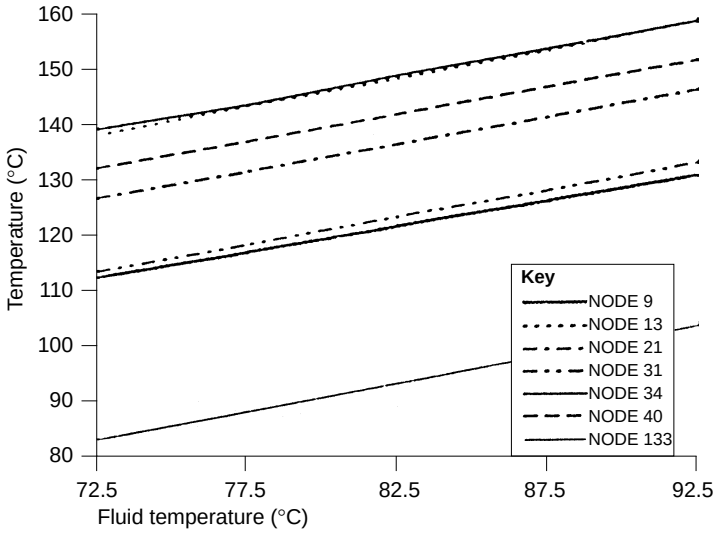

Figure 10.
Effect of inlet fluid temperature

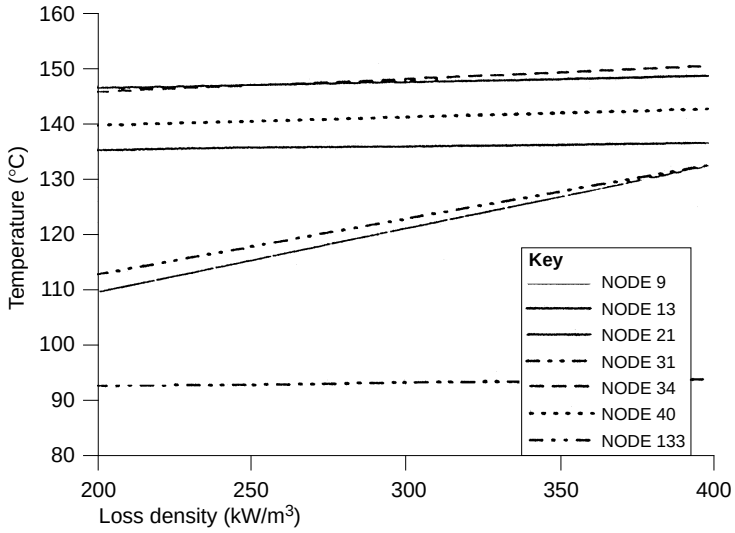

Figure 11.
Effect of rotor winding loss density

to 400kW/m^3 in loss density. The effect on other locations is considerably less. This study will make it possible to simulate the works of earlier researchers who have neglected rotor heating effects and analysed stators in isolation. This clearly shows that the designs neglecting the rotor heating effects will be optimistic and may lead to stator winding failure.

The effect of heat transfer co-efficients in the stator ducts on temperature distribution is shown in Figure 12. It is clear from the figure that it is the interior winding and core temperatures that are affected by changes in heat transfer co-

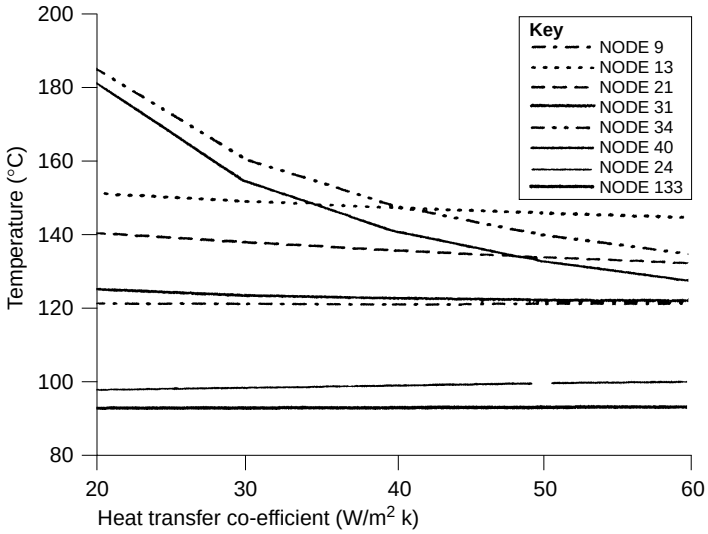

Figure 12.
Effect of stator duct heat transfer co-efficient

efficient. The temperatures of interior stator winding (node 34) and core (node 40) reduce by 30 percent when the heat transfer co-efficient is increased from $20W/m^2K$ to $60W/m^2K$.

7. Summary and conclusions

7.1 Steady state performance

A methodology based on axi-symmetric finite element formulation has been developed to solve the conduction-convection problem in a radial cooled motor using the newly developed eight noded solid-fluid coupled element. A prototype of the radial cooled induction motor has been specially built to validate the numerical results. Heat run tests have been carried out at different loads of 102kW and 77kW at 3,000 rpm to validate the numerical results. The following conclusions are drawn based on the thermal analysis carried out on the machine:

(1) It is observed that the predicted winding temperature agrees well with the measured winding temperature and the variation is of the order of 3 percent. Hence the finite element model can be used for the prediction of steady state thermal performance of a radial cooled motor at the design stage itself.

(2) Predictions show that the hot spots occur at the mid winding region in the full load tests of 102kW and at the mid-core portion in the 77kW load tests.

(3) The numerical model proposed based on the new coupled element is much simpler compared to the traditional method which involves solving the Navier-Stokes and energy equations simultaneously. The proposed method is cost effective and can be solved using any standard PC.

7.2 Parametric studies

The effect of design parameters on the temperature distribution in radial cooled induction motors has been investigated for optimisation and the inferences are given below:

(1) It is observed that the flow parameters affect the temperature distribution the most. An increase in the total flow rate from $0.15m^3/s$ to $0.35m^3/s$ reduces temperatures of stator winding, rotor winding and core by 27 percent at the interior locations and by about 8 percent for locations at the ends.

(2) Another important parameter is the inlet fluid temperature, which forms the boundary condition for the thermal problem. An increase of 20°C in the inlet fluid temperature results in a uniform increase of about 19°C in all the locations.

(3) The temperatures in the rotor winding increase by 21 percent and stator winding by 3.2 percent when the rotor winding loss densities are

increased from 200kW/m^3 to 400kW/m^3. The effect on other locations is considerably less.

(4) The temperatures of interior stator winding and core reduces by as much as 30 percent when the stator duct heat transfer co-efficient is increased from 20W/m^2K to 60W/m^2K.

References

Armor, A.F. and Chari, V.M.K. (1976), "Heat flow in the stator core of large turbine generators by the method of three dimensional finite elements. Part I: Analysis by scalar potential formulation; Part II: Temperature distribution in the stator iron", *IEEE Transactions on PAS*, Vol. 95 No. 5, pp. 1648-68.

Chari, M.V.K and Armor, A.F. (1977), "Combined electro-thermal finite element analysis of turbine generators", *Electrical Machines and Electromechanics*, Vol. 1, pp. 355-64.

Nonaka, S., Yamamoto, M., Nakano, M. and Kawase, M. (1981), "Analysis of ventilation and cooling system for induction motors", *IEEE Transactions on PAS*, Vol. 100 No. 11, pp. 4636-43.

Ohishi, H., Sasake, S. and Yamamura, K. (1987), "Analysis of temperature distribution in coil-strands of rotating electric machines with one turn coil", *IEEE Transactions on EC*, Vol. 2 No. 3, pp. 432-8.

Rajagopal, M.S., Seetharamu, K.N. and Aswatha Narayana, P.A. (1998), "Transient thermal analysis of induction motors", *IEEE Transactions on Energy Conversion*, Vol. 13 No. 1, pp. 62-9.

Stephenson, P.L. (1989), "Calculation of temperature rises due to conductor losses in a radially cooled turbogenerator rotor", *IEE International Conference on Electrical Machines and Drives*, London, September, pp. 150-3.

Williamson, S. and Walker, J.D. (1991), "Calculation of stall bar temperature rise", *5th International Conference on Electrical Machines and Drives*, September, pp. 271-5.

Witczak, P. (1986), "The transient heat flow in stator of the high voltage induction motor", *International Conference on Evolution and Modern Aspects of Induction Machines*, Turin, July, pp. 140-3.

Further reading

Segerlind, L.J. (1984), *Applied Finite Element Analysis*, John Wiley, New York, NY.

Zienkiewicz, O.C. (1971), *The Finite Element Method in Engineering Science*, McGraw-Hill Book Co., London.